



Cite this: *Nanoscale*, 2020, **12**, 5914

Novel layered $\text{Bi}_3\text{MoM}_\text{T}\text{O}_9$ (M_T = Mn, Fe, Co and Ni) thin films with tunable multifunctionalities†

Xingyao Gao,^a Leigang Li,^a Di Zhang,^a Xuejing Wang,^a Jie Jian,^a Zihao He^b and Haiyan Wang  ^{a,b}

$\text{Bi}_3\text{MoM}_\text{T}\text{O}_9$ ($\text{BMoM}_\text{T}\text{O}$; M_T , transition metals of Mn, Fe, Co and Ni) thin films with a layered supercell structure have been deposited on LaAlO_3 (001) substrates by pulsed laser deposition. Microstructural analysis suggests that pillar-like domains with higher transition metal concentration (e.g., Mn, Fe, Co and Ni) are embedded in the Mo-rich matrix with layered supercell structures. The layered supercell structure of the $\text{BMoM}_\text{T}\text{O}$ thin films accounts for the anisotropic multifunctionalities such as the magnetic easy axis along the in-plane direction, and the anisotropic optical properties. Ferroelectricity and ferromagnetism have been demonstrated in the thin films at room temperature, which confirms the multiferroic nature of the system. By varying the transition metal M_T in the film, the band gaps of the $\text{BMoM}_\text{T}\text{O}$ films can be effectively tuned from 2.44 eV to 2.82 eV, while the out-of-plane dielectric constant of the thin films also varies. The newly discovered layered nanocomposite systems present their potential in ferroelectrics, multiferroics and non-linear optics.

Received 4th January 2020,
Accepted 18th February 2020

DOI: 10.1039/d0nr00083c
rsc.li/nanoscale

Introduction

Aurivillius phases, in perovskite-related structures with the formula of $\text{Bi}_2\text{A}_{n-1}\text{B}_n\text{O}_{3n+3}$ (A = Ca, Sr, Ba, Pb, Bi, Na, K, B = Ti, Nb, Ta, Mo, W, Fe),^{1,2} have sparked significant research interest due to their potential applications in piezoelectric devices,^{3–5} superconductors,^{6–8} thermoelectric generators,^{9,10} photocatalysts,^{11,12} etc. In an Aurivillius lattice, n perovskite-like $(\text{Bi}_2\text{A}_{n-1}\text{B}_{3n+1})^{2-}$ layers and one bismuth-oxygen $(\text{Bi}_2\text{O}_2)^{2+}$ layer are stacked alternately,¹³ which generates a unique layered structure and promising properties. Due to the structural differences along the crystallographic orientations that are either parallel or perpendicular to the $(\text{Bi}_2\text{O}_2)^{2+}$ layers, anisotropic properties have been reported in many Aurivillius systems. For example, anisotropic optical properties have been reported in $\text{Bi}_2\text{AlMnO}_6$ supercell (SC) thin films;¹⁴ anisotropic ionic conductivity has been demonstrated in a $\text{Bi}_4\text{V}_{2-x}\text{Co}_x\text{O}_{11-\delta}$ single crystal;¹⁵ and an anisotropic dielectric constant has been observed in a $\text{BaBi}_2\text{Nb}_2\text{O}_9$ system.¹⁶ Besides, the Aurivillius phase has shown low leakage^{17,18} and fatigue free^{19,20} ferroelectric properties at room temperature,

which enable its potential applications in ferroelectric random access memory (FRAMs).²¹

Over the past few decades, considerable attention has been devoted to the exploration of multiferroic materials. Multiferroics are materials that simultaneously possess more than one ferroic characteristics (*i.e.* ferroelectricity, ferromagnetism and ferroelasticity),^{22,23} which can be used in sensors, data storage, high-temperature electronics and memory devices.^{24–26} Perovskite-type oxides with the formula of $\text{AM}_\text{T}\text{O}_3$ (A = Bi, Pb; M_T = transition metal ion) have been demonstrated as candidates for single phase multiferroic materials.²⁷ For example, BiMnO_3 has been reported to be a multiferroic material which has coexisting ferromagnetic and ferroelectric responses.^{28,29} Beside the single phase multiferroic materials, multiphase materials which combine different ferroic orders into one system have been well studied to artificially generate multiferroic properties.^{30–32} Despite the tremendous efforts that have been made for exploring new systems, single phase multiferroic materials are still rare in nature.

In this work, layered Aurivillius phase Bi_2MoO_6 (BMoO) has been incorporated with the perovskite-type transition metal oxides $\text{BiM}_\text{T}\text{O}_3$ ($\text{BM}_\text{T}\text{O}$, M_T = Mn, Fe, Co and Ni) to form a new multiferroic nanocomposite system. BMoO is a ferroelectric material with a high Curie temperature (570 °C),³³ while $\text{BM}_\text{T}\text{O}$ is a multiferroic system as mentioned above. Interestingly, by combining BMoO and $\text{BM}_\text{T}\text{O}$, a new nanocomposite material system ($\text{Bi}_3\text{MoM}_\text{T}\text{O}_9$ or $\text{BMoM}_\text{T}\text{O}$ as the abbreviation) has been created. A layered SC structure, which is similar to the Aurivillius phase, has been observed in this new material

^aSchool of Materials Engineering, Purdue University, West Lafayette, IN 47907, USA.
E-mail: hwang00@purdue.edu

^bSchool of Electrical and Computer Engineering, Purdue University, West Lafayette, IN 47907, USA

† Electronic supplementary information (ESI) available. See DOI: [10.1039/d0nr00083c](https://doi.org/10.1039/d0nr00083c)

system. Meanwhile, pillar-like domains have been generated inside the thin films. Fig. 1(a) shows a 3D schematic drawing of the $\text{BMoM}_\text{T}\text{O}$ thin films, illustrating the pillar like domains embedded in the layered matrix structure. The enlarged schematic illustration demonstrates that the crystal structure consists of the alternately stacked two $\text{Bi}-\text{O}$ layers and one $\text{Mo}/\text{M}_\text{T}-\text{O}$ layer. Besides, the $\text{BMoM}_\text{T}\text{O}$ thin films exhibited tunable multifunctionalities, including room-temperature multiferroic properties (*i.e.* ferroelectricity and ferromagnetism) and optical properties (band gap and dielectric constant). These functionalities are anisotropic due to the layered structure and can be effectively tuned by changing the category of the transition metal in the system.

Results and discussion

X-ray diffraction (XRD) analysis was first performed to characterize the microstructure and growth quality of the thin films. Fig. 1(b) shows the normalized θ - 2θ XRD pattern of the $\text{BMoM}_\text{T}\text{O}$ thin films and pure BMoO thin films grown on LaAlO_3 (LAO) (001) substrates. From the XRD patterns, periodic (00l)-type diffraction peaks can be observed, indicating the high quality SC structure of the thin films with preferential growth along the out-of-plane (OP) direction. Corresponding OP *d*-spacing of the thin films can be calculated using Bragg's law, and all the films have similar lattice parameters of around 8.1 Å, as compared in Fig. S1.[†] This result is predictable from the XRD patterns, where there is no obvious film peak shift for different films, indicating the similar SC structures in $\text{BMoM}_\text{T}\text{O}$ and BMoO thin films. The pure BMoO thin film has sharper peaks with a smaller full width at half maximum (FWHM), indicating higher crystallinity of the pure film compared to that of the thin films. This result might be related to the formation of the domains in the film, which will be discussed further below.

To better understand the microstructure of the $\text{BMoM}_\text{T}\text{O}$ thin films, cross-sectional transmittance electron microscopy

(TEM) was conducted. Fig. 2(a) shows the cross-sectional TEM image of the $\text{Bi}_3\text{MoFeO}_9$ (BMoFeO) thin film grown on an LAO (001) substrate. Overall, the film shows a layered SC structure with the lattice planes parallel to the substrate, as discussed in the XRD pattern analysis. Besides, it is noted that some bright pillar-like domains are formed in the film. These domains might be formed as a result of the atomic composition variation within the film, *i.e.*, the "pillars" are Fe-rich compared to the rest of the film, thus forming the nanopillar-like Fe-rich domains. In the meantime, the "matrix" is Mn-rich. As Fe has a smaller atomic number than Mo, the Fe-rich regions show brighter contrast in the TEM mode. Fig. 2(b) shows the corresponding SAED pattern taken along the [100] zone axis. Distinguished diffraction dots in the SAED pattern indicate the highly epitaxial growth of the BMoFeO SC structure and confirm the (00l) growth direction of the layered thin films. Fig. 2(c) shows a scanning transmittance electron microscopy (STEM) image of the BMoFeO film taken under the high angle annular dark field (HAADF) mode of the same area which shows a clear SC structure with the same domain structure but with inverted contrast. STEM under HAADF mode is also called Z-contrast and the image contrast is proportional to Z^2 . The Fe-rich and Mo-rich domains are marked by the yellow and purple arrows, respectively. Fig. 2(d) shows an HRSTEM image of the sample taken at the domain boundary area, where the black dashed line represents the boundary between the Fe-rich domain (dark contrast due to a lower atomic number) and Mo-rich domain (brighter contrast due to a higher atomic number). The film shows an obvious Aurivillius structure with alternately aligned $\text{Bi}-\text{O}$ layers and $\text{Mo}/\text{M}_\text{T}-\text{O}$ layer, as shown in Fig. 1(a). It is interesting to note that the horizontal SC layers are continuous throughout the domain boundaries, which proves that the domains in the BMoFeO thin film are formed by the compositional differences, instead of crystal structure differences. Fig. S2[†] shows a fast-Fourier transform (FFT) filtered image obtained from the selected area in the HRSTEM image, where there is no dislocation observed

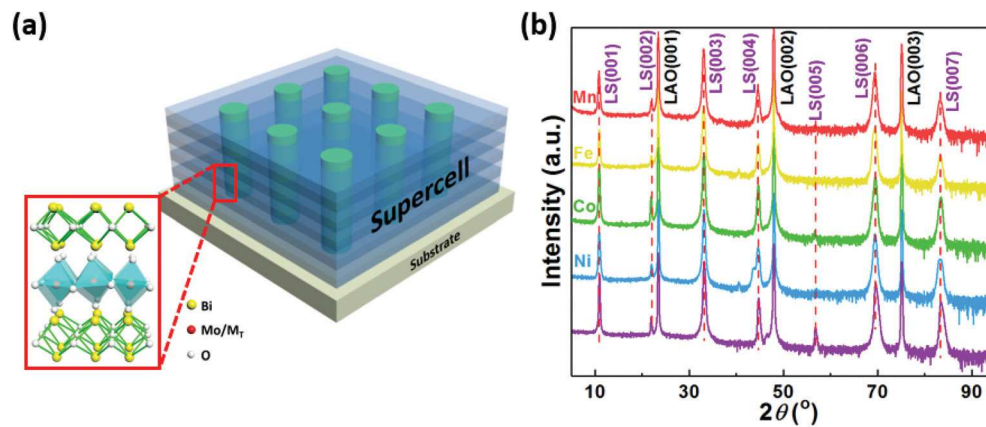


Fig. 1 (a) 3D schematic drawing of the $\text{BMoM}_\text{T}\text{O}$ thin films with pillar like domains embedded in a matrix structure. The enlarged schematic illustration demonstrates that the film consists of alternately stacked two $\text{Bi}-\text{O}$ layers and one $\text{Mo}/\text{M}_\text{T}-\text{O}$ based layer. (b) θ - 2θ XRD scans of $\text{BMoM}_\text{T}\text{O}$ and BMoO thin films. The red dashed lines indicate the positions of the (00l) peaks.

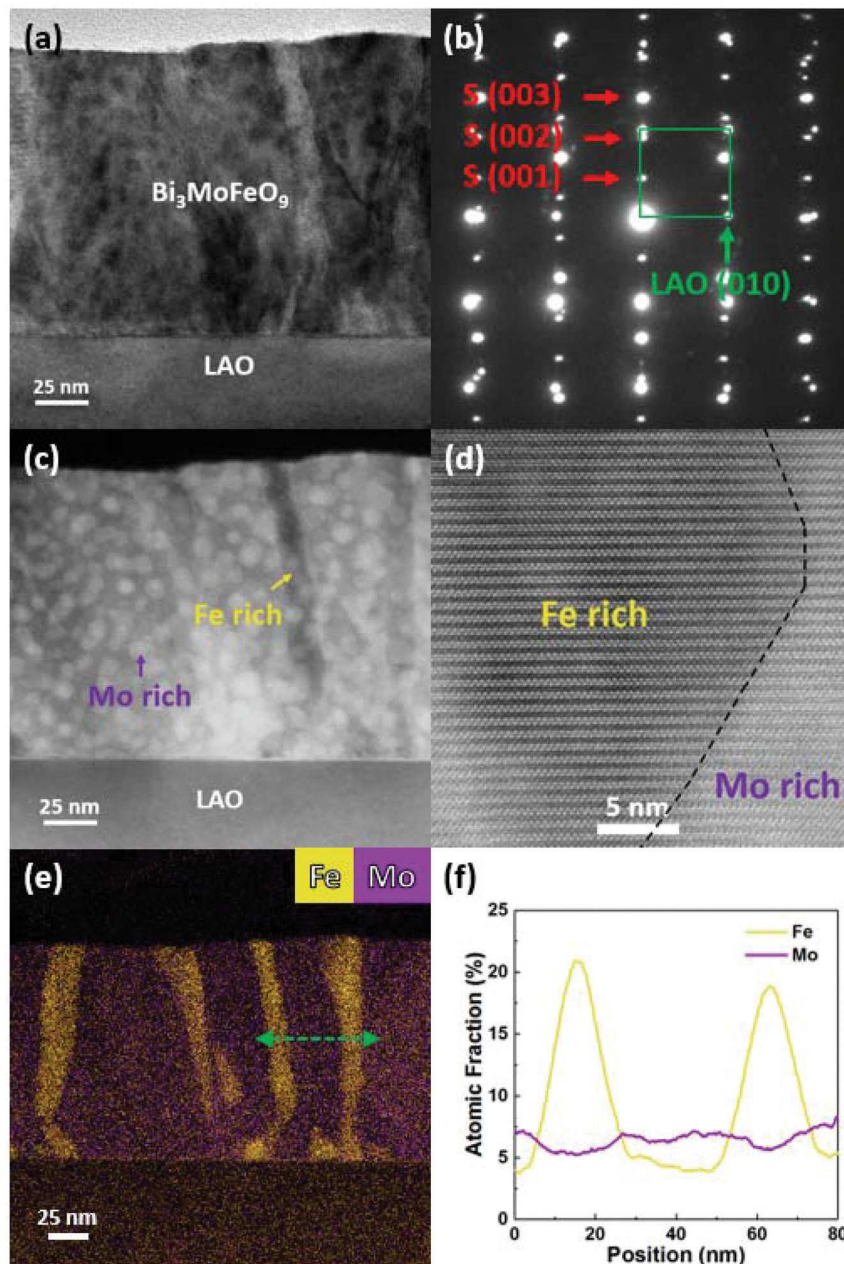


Fig. 2 (a) Cross-sectional TEM image and (b) selected area electron diffraction (SAED) pattern and (c) STEM image of the BMoFeO thin film. (d) HRTEM image of the BMoFeO thin film, while the black dashed line indicates the domain boundary. (e) Cross-sectional energy-dispersive X-ray spectroscopy (EDS) mapping of Fe (yellow) and Mo (purple) atoms in the BMoFeO film. The green arrow indicates the selected area for (f) smoothed linear EDS analysis of the Fe and Mo atoms.

at the grain boundary, which again demonstrates the continuity of the SC structure across the domain boundaries. This observed phenomenon explains why there is no secondary phase peak in the XRD pattern shown in Fig. 1(b). Similar results have been observed in films with other compositions, such as $\text{Bi}_3\text{MoMnO}_9$ (BMoMnO), $\text{Bi}_3\text{MoCoO}_9$ (BMoCoO) and $\text{Bi}_3\text{MoNiO}_9$ (BMoNiO), as shown in Fig. S3.† Fig. 2(e) shows the corresponding cross-sectional EDS mapping of the BMoFeO thin film, where the Fe and Mo elements are marked

in yellow and purple, respectively. This image shows clear Fe-rich pillar-like domains embedded in the Mo rich matrix. An EDS line scan at the green arrow marked region in Fig. 2(f) shows the Fe and Mo distribution, marked in yellow and purple, respectively. Both elements exist in the entire scanned region, while Fe shows an obvious composition jump in the pillar area, which confirms the Fe-rich pillar area. The atomic fraction of Mo is higher in the Mo-rich matrix area compared to that in the pillars. This result confirms that the domains in

the BMoFeO thin film are formed by the distribution of Fe and Mo atoms. In BMoM_TO thin films, the Mo and M_T atoms in the Mo/M_T layers occupy equivalent positions within the unit cells, while the atomic ratios of the Mo and M_T atoms vary in different regions. This variation generates different domains shown in EDS mapping, but the layered structure is maintained across the domain boundaries. As the cross-sectional EDS only shows very localized information and the EDS composition is for estimation, the sum of the Mo and Fe atomic ratios varies slightly across the green arrow. Besides, the dark and bright contrast areas observed in the TEM and STEM images might be due to the local non-uniform elemental distribution and the non-uniformity is minor, which is originated from the TEM sample preparation.

Piezoresponse force microscopy (PFM) measurements were performed to explore the electrical properties of the BMoM_TO thin films, as shown in Fig. 3. SrRuO_3 (SRO) buffer layers were grown first as the bottom electrodes. The left panel of each figure shows the phase (plotted in blue) and amplitude (plotted in red) switching curves of BMoM_TO with different M_T elements (Mn, Fe, Co and Ni, respectively). For all four films, the phase curves show obvious hysteresis loops with 180° phase switching when the bias directions are switched and the amplitude curves show a butterfly-like shape. These curves indicate the ferroelectric nature of the BMoM_TO thin films. The right panels of the figures show the OP phase switching images after writing and re-writing processes, where the positive tip biases were first applied on $0.5 \times 0.5 \mu\text{m}^2$ areas followed by the negative tip biases applied on $0.2 \times 0.2 \mu\text{m}^2$ areas. After the writing and re-writing processes, distinct phase switching can be observed, which further confirms the ferroelectric properties in all the BMoM_TO thin films. All the above

measurements were conducted at 300 K, demonstrating the room temperature ferroelectric nature of the BMoM_TO thin films. It has been previously reported that the ferroelectricity in BMoO thin films is due to the displacement of the Mo cations in the non-central symmetry crystal lattice;³³ therefore the room temperature ferroelectric properties of the BMoM_TO thin films might have originated from the displacement of both Mo and M_T cations and the non-central symmetry lattice structure.

To explore the magnetic properties of the BMoM_TO thin films, ferromagnetic hysteresis loops were obtained using the magnetic property measurement system (MPMS). Fig. 4(a) and (b) show the room temperature M - H curves of the BMoM_TO thin films with the magnetic fields applied in-plane (IP) and OP, respectively. The insets of the figures illustrate the directions of the applied fields. As shown in the figures, the BMoM_TO thin films show strong ferromagnetic properties at room temperature, in both IP and OP directions. As a comparison, the pure BMoO film only shows very weak magnetic response, as plotted in Fig. S4.[†] The huge enhancement of the magnetic response in the BMoM_TO thin films is attributed to the incorporation of the magnetic elements M_T (e.g., Mn, Fe, Co and Ni). Interestingly, the IP anisotropic magnetic properties, i.e., stronger magnetic response in the IP direction, have been observed in most of the BMoM_TO thin films, including BMoFeO , BMoMnO and BMoNiO , which is possibly due to the easy IP magnetocrystalline axis for the layered structure, similar to the pure BMoO case. Differently, the BMoCoO sample shows better ferromagnetic response along the OP direction. This might be related to the poorer film quality (as shown in Fig. S3(f)[†]) which results in the OP anisotropy. The ferromagnetic property variation in BMoM_TO films might have

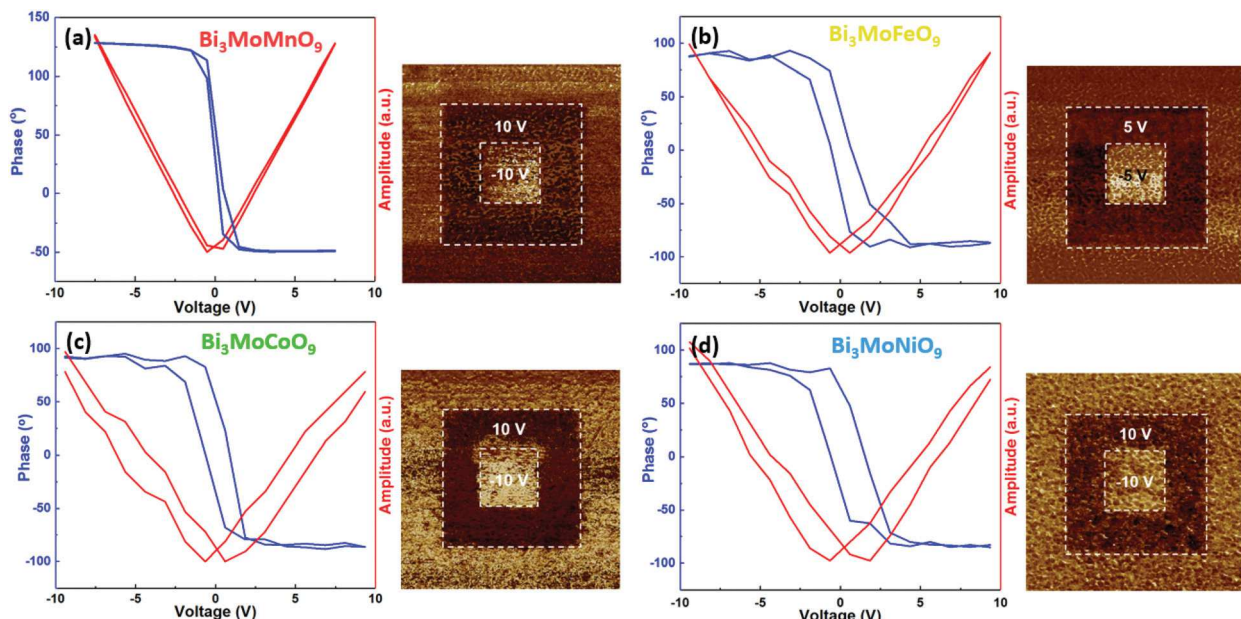


Fig. 3 (a–d) Left panels: The phase (blue) and amplitude (red) switching curves of the BMoM_TO thin films; right panels: PFM phase image of the BMoM_TO films with different elements (Mn, Fe, Co and Ni, respectively).

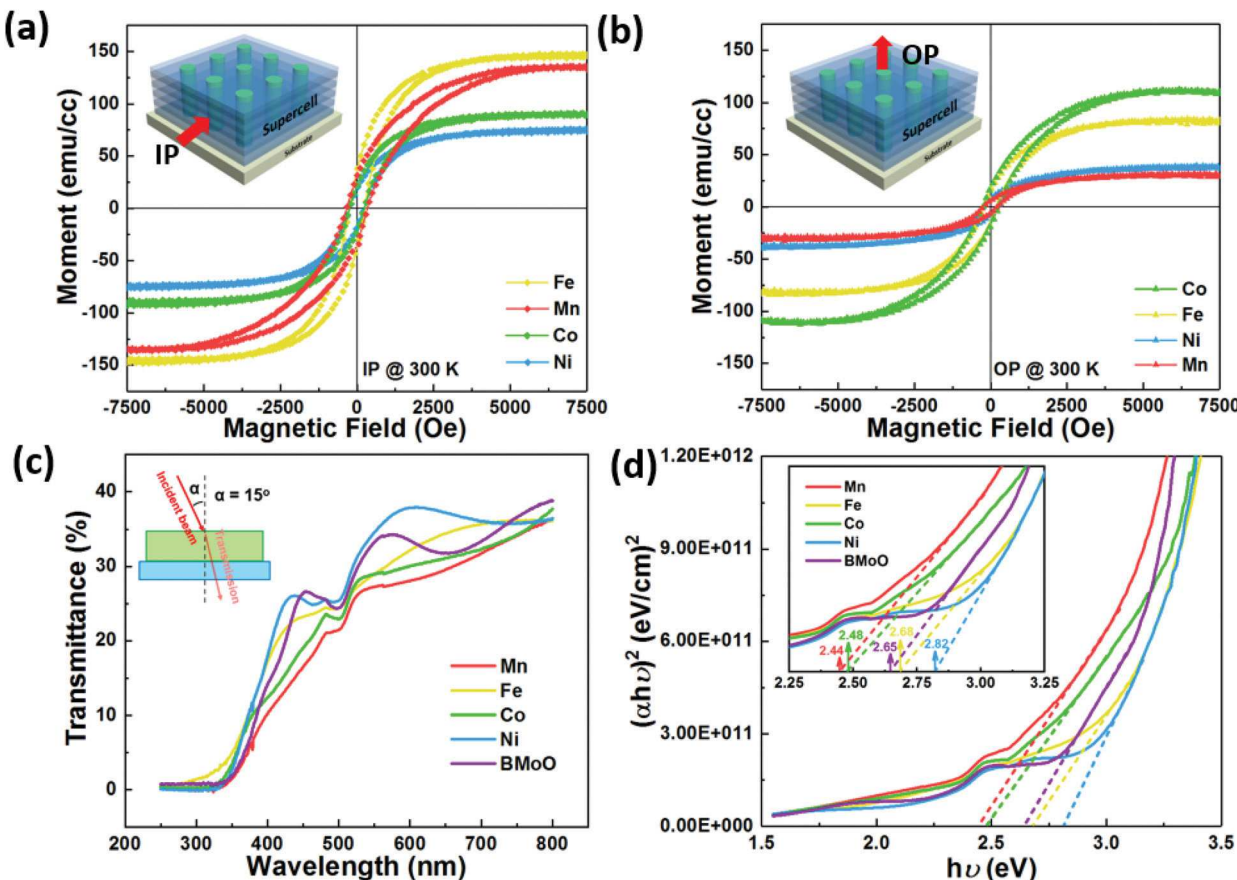


Fig. 4 (a) In-plane and (b) out-of-plane magnetic hysteresis loops of BMoM_TO films measured at 300 K. The insets show the corresponding magnetic field directions. (c) The optical transmittance spectra of the BMoM_TO thin films as a function of the wavelength, with an incident beam angle of 15°. (d) Direct band gaps of the BMoM_TO and BMoO thin films with the inset showing the enlarged figure and the values of the band gaps.

resulted from the different dopant elements in the films and the change of the domain structure. Overall, the coexistence of ferroelectricity and ferromagnetism at room temperature demonstrates the room temperature multiferroic properties of all the BMoM_TO thin films.

Tunable optical responses in BMoM_TO thin films are also expected because of the various M_T dopants and the unique nanopillar-in-matrix structures. First, transmittance measurements were conducted. Fig. 4(c) shows the optical transmittance spectra of the BMoM_TO thin films as a function of the wavelength. The corresponding direct band gaps of each film were calculated using the Tauc method, and results are shown in Fig. 4(d) with an inset showing the enlarged plot labelling the band gaps of each film. The band gap of the BMoO thin films is estimated to be 2.65 eV, which is comparable to previously reported values.^{34–36} By changing magnetic elements M_T in the system, tunable direct band gaps of the BMoM_TO thin films ranging from 2.44 eV to 2.82 eV were obtained for Mn, Co, pure, Fe, and Ni. This tuning result might be attributed to the minor structural change based on the ionic size reduction of M_T ions in the lattice, as well as the shape, size and density of the pillar domains. The angular dependence of the transmittance spectra has been studied and is shown in

Fig. S5.† It can be observed that the on-set points (marked by the arrows) shift to the left as the incident beam angle increases. The shift of the on-set points *versus* the incident beam angles suggests the anisotropic nature of the optical properties in the BMoM_TO thin films, which originates from the layered structure of the Aurivillius phase thin films.¹⁴ The peaks observed at around 480 nm are the errors caused by the detector.

Ellipsometry experiments were conducted to further explore the anisotropic optical properties of the BMoM_TO thin films. Fig. 5(a–e) show the fitted real dielectric constants of the thin films in both the IP (ϵ_{\parallel} marked with dashed lines) and OP (ϵ_{\perp} marked with solid lines) directions. It can be seen that the IP dielectric constants of the BMoM_TO thin films have similar values and trend compared to those of the pure BMoO thin film, while the OP dielectric constants vary drastically with the film compositions. All the OP dielectric constants are plotted in Fig. 5(f) for better comparison. More specifically, the OP dielectric constant (ϵ_{\perp}) decreases from Co, Mn, Fe, and pure BMoO, to Ni. This leads to OP anisotropy in the Co and Mn cases and IP anisotropy in the pure BMoO, Fe and Ni cases. The tunable optical dielectric properties result from the structures. For IP, the layered structure dominates the electronic

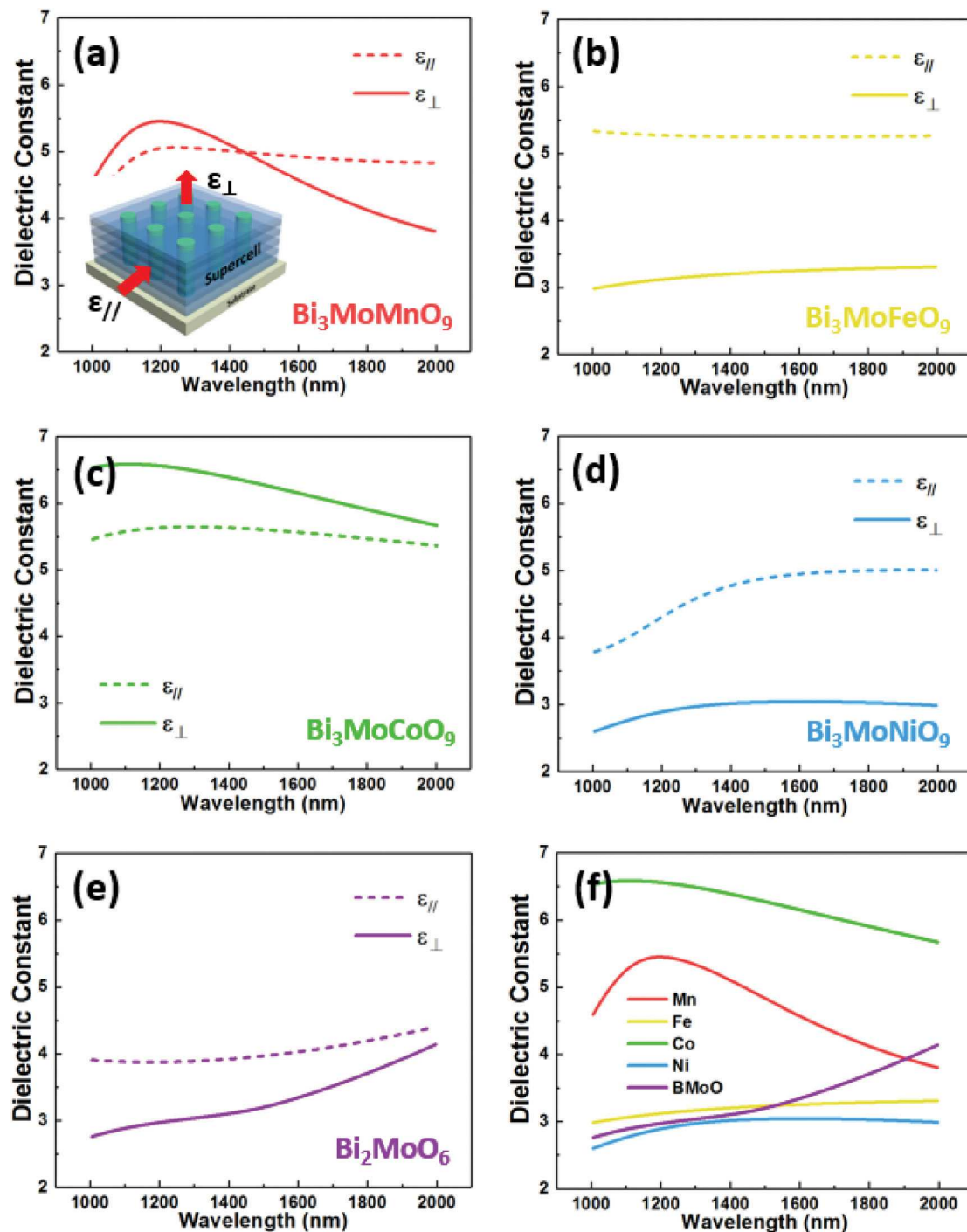


Fig. 5 (a–e) Fitted real dielectric constants of the BMoMnO_9 and BMoO_6 thin films in both the in-plane (marked with dashed lines) and out-of-plane (marked with solid lines) directions. (f) Comparison of the out-of-plane dielectric constants of the BMoMnO_9 and BMoO_6 thin films.

density of states and the light–matter interactions IP and thus results in a very similar IP (ϵ_{\parallel}) constant. For OP, depending on the secondary dopants and the structural variation, the density of states in the samples varies and thus results in the largely different OP dielectric constant (ϵ_{\perp}). The results of the ellipsometry experiments have demonstrated the tunable optical properties such as the OP dielectric constant and overall optical

dielectric anisotropy properties. Due to the equipment limitation, the dielectric constants at the bandgap regimes were noisy and thus are excluded from the figures.

In this work, the design and fabrication of new nanocomposites by combining an Aurivillius phase material with a perovskite-type transition metal oxide in a unique nanopillar-in-matrix form provide an effective approach of exploring new

materials systems using layered SC structures. The advantages of the compositionally varied domains, instead of the completely different secondary phases, include the following: (1) high quality layered nanocomposite structures were maintained without much film quality deterioration due to secondary phase growth; (2) novel layered oxide properties remain dominant in IP, such as ferroelectric properties and nonlinearity, while the OP properties are tunable depending on the secondary dopant in the systems; and (3) highly anisotropic physical properties can be achieved easily in these layered nanocomposite systems by proper selection of the secondary phases, which provides large flexibility in nanocomposite designs and property tuning.

Conclusions

$\text{Bi}_3\text{MoM}_\text{T}\text{O}_9$ (BMoM_TO, M_T = Mn, Fe, Co and Ni), a new oxide nanocomposite system with an SC layered structure as the matrix has been grown on LAO (001) substrates by the pulsed laser deposition (PLD) technique. The thin films have pillar-like domains (M_T-rich) embedded in the matrix (Mo-rich). Instead of forming dislocations and other interfacial defects, the atomic lattices are continuous across the domain boundaries. Room temperature multiferroic properties (*i.e.* ferroelectricity and ferromagnetism) have been demonstrated in the new systems. Anisotropic multifunctionalities, including ferromagnetism, optical transmittance and dielectric anisotropy, have been demonstrated as a function of the secondary phase composition M_T. As the film composition (*i.e.* M_T) varies, the magnetic anisotropy, optical bandgap, and dielectric function can be effectively tuned. These tunable multifunctionalities in these layered oxide nanocomposite systems present promising applications toward sensors, data storage, high-temperature electronics, memory devices and non-linear optical devices.

Experimental section

The BMoM_TO targets and a pure BMoO target were prepared by conventional solid-state sintering methods. The thin films were deposited onto single crystal LaAlO_3 (LAO) (001) substrates using pulsed laser deposition (PLD, KrF, $\lambda = 248$ nm) with an optimized substrate temperature of 600 °C and an oxygen pressure of 200 mTorr during the thin film growth. After the deposition, the as-deposited samples were cooled down to 400 °C at a rate of 5 °C min⁻¹ under a 500 Torr oxygen atmosphere and subsequently annealed for one hour to reduce the oxygen vacancies. SrRuO_3 (SRO) buffer layers were firstly deposited onto the substrates as bottom electrodes for ferroelectric measurements. The microstructure of the fabricated thin films were investigated by X-ray diffraction (XRD, PANalytical Empyrean) and transmission electron microscopy (TEM, Thermo Scientific TALOS F200X and Thermo Scientific TEAM 1). The piezoelectric properties were measured by atomic force microscopy (AFM, Bruker Dimension Icon) and

piezoresponse force microscopy (PFM) with a conductive Pt-Ir coated Si tip (SCM-PIT). The magnetic properties were investigated using a magnetic property measurement system (MPMS, Quantum Design MPMS-3) with the magnetic field applied in both the in-plane (IP) and out-of-plane (OP) directions. The normal incident depolarized transmittance (T%) of the films were carried using an optical spectrophotometer (Lambda 1050 UV/Vis Spectrophotometer) with a spectrum range of 250–800 nm and incident angles of 15°, 30°, 45°, 60° and 75°, respectively. The direct band gaps were estimated by the Tauc method from the transmittance result obtained at 15°. The ellipsometry experiments were performed on an RC2 spectroscopic ellipsometer (J.A. Woollam Company) with a spectrum range of 1000–2000 nm and three angles of 50°, 60° and 70°. The real dielectric constants of the thin films were then retrieved from the software (CompleteEase, J.A. Woollam Company) using the Spline or Gen-Osc model.

Conflicts of interest

There are no conflicts to declare.

Acknowledgements

This work is supported by the U.S. Office of Naval Research (N00014-16-1-2465) for thin film growth and U.S. National Science Foundation (DMR-1565822) for HR(S)TEM work. J. J. and D. Z. acknowledge the partial support from the U.S. Office of Naval Research (N00014-20-1-2043). Z. H. acknowledges the support from the U.S. National Science Foundation (DMR-1809520).

References

- 1 B. Frit and J. P. Mercurio, The crystal chemistry and dielectric properties of the Aurivillius family of complex bismuth oxides with perovskite-like layered structures, *J. Alloys Compd.*, 1992, **188**, 27–35.
- 2 L. Zhang, W. Wang, M. Shang, S. Sun and J. Xu, Bi_2WO_6 @carbon/Fe₃O₄ microspheres: Preparation, growth mechanism and application in water treatment, *J. Hazard. Mater.*, 2009, **172**, 1193–1197.
- 3 H. Yan, *et al.*, The effect of (Li, Ce) and (K, Ce) doping in Aurivillius phase material CaBi₄Ti₄O₁₅, *Mater. Res. Bull.*, 2004, **39**, 1237–1246.
- 4 H. Du and X. Shi, Dielectric and piezoelectric properties of barium-modified Aurivillius-type Na_{0.5}Bi_{4.5}Ti₄O₁₅, *J. Phys. Chem. Solids*, 2011, **72**, 1279–1283.
- 5 T. Jardiel, A. C. Caballero and M. Villegas, Aurivillius ceramics: Bi₄Ti₃O₁₂-based piezoelectrics, *J. Ceram. Soc. Jpn.*, 2008, **116**, 511–518.
- 6 R. L. Withers, *et al.*, A transmission electron microscope and group theoretical study of the new Bi-based high-T_c

superconductors and some closely related Aurivillius phases, *J. Phys. C: Solid State Phys.*, 1988, **21**, 6067–6083.

7 J. K. Liang, *et al.*, Crystal Structure and Superconductivity of $\text{Bi}_2\text{Sr}_2\text{CaCu}_2\text{O}_8$ Compound, *Mod. Phys. Lett. B*, 1988, **2**, 483–489.

8 K. A. Yee, T. A. Albright, D. Jung and M. Whangbo, Aurivillius Phases : A Possible New Class of Metal Oxide Superconductors, *Angew. Chem., Int. Ed. Engl.*, 1989, **28**, 750–751.

9 H. Kohri, M. Kato, I. J. Ohsugi and I. Shiota, Thermoelectric Generating Properties of Perovskite Like Materials, *Adv. Sci. Technol.*, 2010, **74**, 72–76.

10 H. Kohri and T. Yagasaki, Thermoelectric Generating Properties of Aurivillius Compounds, *Adv. Sci. Technol.*, 2012, **77**, 285–290.

11 G. Naresh and T. K. Mandal, Excellent Sun-Light-Driven Photocatalytic Activity by Aurivillius Layered Perovskites, $\text{Bi}_{5-x}\text{La}_x\text{Ti}_3\text{FeO}_{15}$ ($x = 1,2$), *ACS Appl. Mater. Interfaces*, 2014, **6**, 21000–21010.

12 B. Muktha, M. H. Priya, G. Madras and T. N. G. Row, Synthesis, Structure, and Photocatalysis in a New Structural Variant of the Aurivillius Phase: $\text{LiBi}_4\text{M}_3\text{O}_{14}$ ($\text{M} = \text{Nb, Ta}$), *J. Phys. Chem. B*, 2005, **109**, 11442–11449.

13 K. R. Kendall, C. Navas, J. K. Thomas and H. zur Loye, Recent Developments in Oxide Ion Conductors: Aurivillius Phases, *Chem. Mater.*, 1996, **8**, 642–649.

14 L. Li, *et al.*, Novel Layered Supercell Structure from $\text{Bi}_2\text{AlMnO}_6$ for Multifunctionalities, *Nano Lett.*, 2017, **17**, 6575–6582.

15 S. Kim and M. Miyayama, Anisotropy in oxide ion conductivity of $\text{Bi}_4\text{V}_{2-x}\text{Co}_x\text{O}_{11-\delta}$, *Solid State Ionics*, 1997, **104**, 295–302.

16 H. Yan, *et al.*, Orientation dependence of dielectric and relaxor behaviour in Aurivillius phase $\text{BaBi}_2\text{Nb}_2\text{O}_9$ ceramics prepared by spark plasma sintering, *J. Mater. Sci.: Mater. Electron.*, 2006, **17**, 657–661.

17 Y. Ahn, J. D. Seo and J. Y. Son, Ferroelectric domain structures of epitaxial $\text{CaBi}_2\text{Nb}_2\text{O}_9$ thin films on single crystalline Nb doped (100) SrTiO_3 substrates, *J. Cryst. Growth*, 2015, **422**, 20–23.

18 C. Long, H. Fan, M. Li, G. Dong and Q. Li, Crystal structure and enhanced electromechanical properties of Aurivillius ferroelectric ceramics, $\text{Bi}_4\text{Ti}_{3-x}(\text{Mg}_{1/3}\text{Nb}_{2/3})_x\text{O}_{12}$, *Scr. Mater.*, 2014, **75**, 70–73.

19 C. A.-P. Araujo, J. D. de Cuchlaro, L. D. McMillan, M. C. Scott and J. F. Scott, Fatigue-free ferroelectric capacitors with platinum electrodes, *Nature*, 1995, **374**, 627–629.

20 H. N. Al-Shareef, D. Dimos, T. J. Boyle, W. L. Warren and B. A. Tuttle, Qualitative model for the fatigue-free behavior of $\text{SrBi}_2\text{Ta}_2\text{O}_9$, *Appl. Phys. Lett.*, 1996, **68**, 690–692.

21 B. H. Park, *et al.*, Lanthanum-substituted bismuth titanate for use in non-volatile memories, *Nature*, 1999, **401**, 682–684.

22 W. Eerenstein, N. D. Mathur and J. F. Scott, Multiferroic and magnetoelectric materials, *Nature*, 2006, **442**, 759–766.

23 W. Prellier, M. P. Singh and P. Murugavel, The single-phase multiferroic oxides : from bulk to thin film, *J. Phys.: Condens. Matter*, 2005, **17**, 803–832.

24 J. F. Scott, Data Storage: Multiferroic Memories, *Nat. Mater.*, 2007, **6**, 256–258.

25 R. Ramesh and N. A. Spaldin, Multiferroics: progress and prospects in thin films, *Nat. Mater.*, 2007, **6**, 21–29.

26 A. K. Zvezdin, A. S. Logginov, G. A. Meshkov and A. P. Pyatakov, Multiferroics: Promising Materials for Microelectronics, Spintronics, and Sensor Technique, *Bull. Russ. Acad. Sci.: Phys.*, 2007, **71**, 1561–1562.

27 Y. Uratani, T. Shishidou and T. Oguchi, First-Principles Study on the Magnetic Anisotropy in Multiferroic PbVO_3 and BiCoO_3 , *J. Phys. Soc. Jpn.*, 2009, **78**, 084709.

28 L. Zhai and H. Wang, The magnetic and multiferroic properties in BiMnO_3 , *J. Magn. Magn. Mater.*, 2017, **426**, 188–194.

29 H. Jeen, *et al.*, Growth and characterization of multiferroic BiMnO_3 thin films, *J. Appl. Phys.*, 2011, **109**, 074104.

30 H. Wang, *et al.*, Two-Phase Room-Temperature Multiferroic Nanocomposite with BiMnO_3 -Tilted Nanopillars in the $\text{Bi}_2\text{W}_{1-x}\text{Mn}_x\text{O}_6$ Matrix, *ACS Appl. Mater. Interfaces*, 2019, **11**, 26261–26267.

31 H. Wang, *et al.*, Multiferroic vertically aligned nanocomposite with CoFe_2O_4 nanocones embedded in layered Bi_2WO_6 matrix, *Mater. Res. Lett.*, 2019, **7**, 418–425.

32 X. Gao, *et al.*, Vertically Aligned Nanocomposite BaTiO_3 : YMnO_3 Thin Films with Room Temperature Multiferroic Properties toward Nanoscale Memory Devices, *ACS Appl. Nano Mater.*, 2018, **1**, 2509–2514.

33 I. H. Ismailzade, I. M. Aliyev, R. M. Ismailov, A. I. Alekberov and D. A. Rzayev, Ferroelectricity in Bi_2MoO_6 , *Ferroelectrics*, 1979, **22**, 853–854.

34 M. Zhang, *et al.*, One-dimensional $\text{Bi}_2\text{MoO}_6/\text{TiO}_2$ hierarchical heterostructures with enhanced photocatalytic activity, *CrystEngComm*, 2012, **14**, 605–612.

35 V. Umapathy, A. Manikandan, S. A. Antony, P. Ramu and P. Neeraja, Structure, morphology and opto-magnetic properties of Bi_2MoO_6 nano-photocatalyst synthesized by sol–gel method, *Trans. Nonferrous Met. Soc. China*, 2015, **25**, 3271–3278.

36 W. Yin, W. Wang and S. Sun, Photocatalytic degradation of phenol over cage-like Bi_2MoO_6 hollow spheres under visible-light irradiation, *Catal. Commun.*, 2010, **11**, 647–650.